Article:
Li, L., Andrews, J., Mitchell, R. et al. (2023) Aqueous cold sintering of Li-based compounds. ACS Applied Materials & Interfaces, 15 (16). pp. 20228-20239. ISSN: 1944-8244

https://doi.org/10.1021/acsami.3c00392

ACS APPLIED MATERIALS & INTERFACES

www.acsami.org

Research Article

Aqueous Cold Sintering of Li-Based Compounds

Linhao Li, Jessica Andrews, Ria Mitchell, Daniel Button, Derek C. Sinclair, and Ian M. Reaney*

Cite This: *ACS Appl. Mater. Interfaces* 2023, 15, 20228−20239

Read Online

ACCESS | Metrics & More | Article Recommendations | Supporting Information

ABSTRACT: Aqueous cold sintering of two lithium-based compounds, the electrolyte $Li_{6.25}La_3Zr_2Al_{0.25}O_{12}$ (LLZAO) and cathode material $LiCoO_2$ (LCO), is reported. For LLZAO, a relative density of ∼87% was achieved, whereas LCO was sintered to ∼95% with 20 wt % LLZAO as a flux/binder. As-cold sintered LLZAO exhibited a low total conductivity (10^{-8} S/cm) attributed to an insulating grain boundary blocking layer of Li_2CO_3. The blocking layer was reduced with a post-annealing process or, more effectively, by replacing deionized water with 5 M LiCl during cold sintering to achieve a total conductivity of ∼3 × 10^{-5} S/cm (similar to the bulk conductivity). For LCO-LLZAO composites, scanning electron microscopy and X-ray computer tomography indicated a continuous LCO matrix with the LLZAO phase evenly distributed but isolated throughout the ceramics. [001] texturing during cold sintering resulted in an order of magnitude difference in electronic conductivity between directions perpendicular and parallel to the *c*-axis at room temperature. The electronic conductivity (∼10^{-2} S/cm) of cold sintered LCO-LLZAO ceramics at room temperature was comparable to that of single crystals and higher than those synthesized via either conventional sintering or hot pressing.

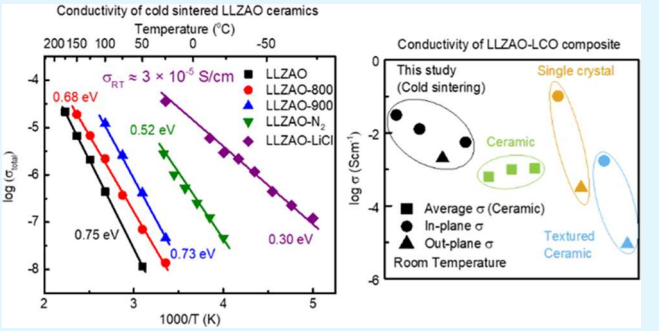

KEYWORDS: *LLZO, LCO, cold sintering, solid electrolyte, ceramic composite, prefer orientation, textured ceramic*

INTRODUCTION

Interest in Li-ion compounds has surged over the last few decades, mainly driven by the development of various types of Lithium-Ion Batteries (LIBs). The use of solid-state electrolytes (SSEs) in LIBs is considered to improve battery safety and potentially achieve high power and energy density over a wide voltage and temperature window.[1,2] However, due to the active chemical nature and volatility of lithium, the processing of Li compounds, especially oxides which require high temperatures for densification, is challenging.

Cold sintering is a newly developed low-temperature consolidation method for ceramics.[3,4] It is pressure-assisted in the presence of a transient liquid phase that enables a dissolution−precipitation sintering mechanism.[5] Due to its low temperature (<300 °C), cold sintering significantly reduces the energy consumed in densification compared with other routes.[6] It also allows integration to high-density dissimilar materials such as ceramics and polymers. Since the first comprehensive publications on this technique in 2016 by Guo et al., it has drawn significant attention across various disciplines such as microwave ceramics, semiconducting oxides, ferroelectrics, ionic conductors, and Li battery materials.[7−21]

The garnet-structured $Li_7La_3Zr_2O_{12}$ (LLZO) is widely regarded as one of the most promising candidates as SSE,[22,23] with its cubic polymorph (∼10^{-3} S/cm) more than two orders of magnitude more conductive than tetragonal polymorph (∼10^{-5} S/cm) in optimized ceramics.[24−26] Consequently, most research has focused on stabilization of the cubic over the tetragonal polymorph, which may be achieved by using dopants on either the Li- (Al^{3+}, Y^{3+}, Ga^{3+}, Fe^{3+}) or the Zr-site (Nb^{+5}, Ta^{+5}, Sb^{+5}).[27−36] Unfortunately, conventional sintering requires 1000−1200 °C, often over long periods of time (up to 36 h in some studies), which subsequently leads to significant Li loss, secondary phases, and reduced density.[33,35,37] Li loss may be compensated by adding extra Li_2CO_3 to the starting composition and/or using sacrificial powder(s), but the precise Li concentration remains an unknown variable (often graded from interior to exterior of the pellet) that is influential in controlling both the structure and ionic conductivity of LLZO.[38−41] As a result, the highest values of conductivity for LLZO are only typically achieved in hot-pressed samples, which avoid Li loss by densifying within a closed system.

$LiCoO_2$ (LCO) is a cathode material reported initially by Goodenough et al.[42,43] Its high conductivity and stable structure still offer high energy density in comparison with

Received: January 10, 2023
Accepted: March 30, 2023
Published: April 13, 2023

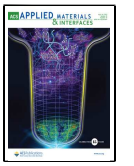

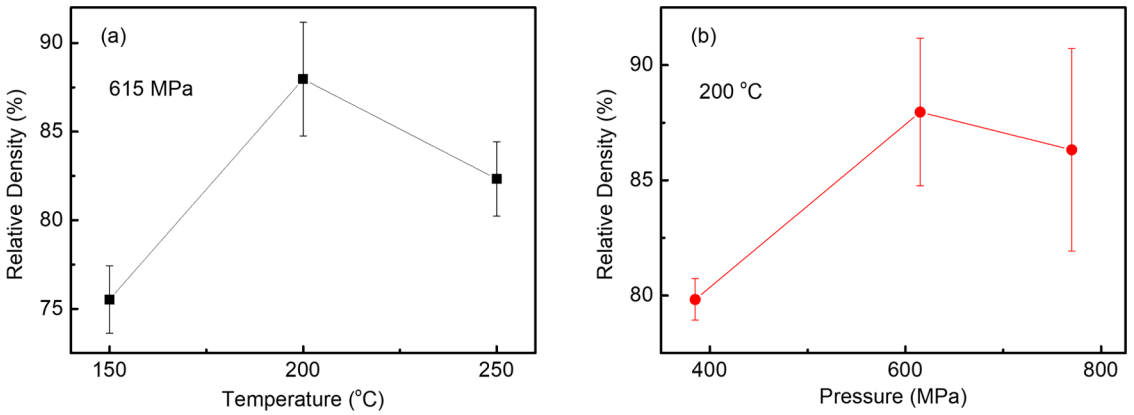

Figure 1. Relative density of the LLZAO ceramics sintered using various (a) pressures and (b) temperatures with deionized water.

newly proposed cathode materials such as $LiMn_2O_4$, $LiFePO_4$, $LiNi_{1-x-y}Co_xMn_yO_2$ ($0 < x, y < 1$), $LiNi_{0.80}Co_{0.15}Al_{0.05}O_2$, and $xLi_2MnO_3{\cdot}(1-x)LiMO_2$ (M = Ni, Co, Mn, etc.).[44−52] LCO possesses a layered rock salt structure (α-$NaFeO_2$ type), which gives rise to its plate-like morphology and anisotropic conductivity that can differ by a factor of ∼500 between in-plane (a, b plane) and out-plane (*c*-axis) orientations based on single-crystal studies.[53] As conductivity is critical for cathode materials, it is desirable to obtain textured LCO, which, until now, has been achieved either by processing a slurry in a strong magnetic field (e.g., 12 T)[54,55] or via hot pressing.[56] The former utilizes the magnetic anisotropy of LCO, whereas the latter is achieved through the application of high pressure and its action on the plate-like morphology.

There are generally two different approaches to the cold sintering of LLZO involving either aqueous[57] or organic (e.g., dimethylformamide, DMF) transient solvents.[21] Although relatively high density (80−90%) LLZO ceramics can be achieved, these two approaches have their own disadvantage. Aqueous cold sintering has been reported to give conductivity 3−4 orders of magnitude lower than optimized hot-pressed LLZO,[54] whereas DMF is toxic, which adds process complexity for scale-up. In contrast, there are no reports of cold sintering of LCO despite its extensive use within the Li-ion battery technology.

In this study, $Li_{6.25}La_3Zr_2Al_{0.25}O_{12}$ (LLZAO) was cold sintered to ∼87% relative density to give an optimized total conductivity of $\sim 3 \times 10^{-5}$ S/cm, close to that of the bulk using a LiCl solution rather than pure water as the transient solvent. LLZAO was then used as a flux/binder to aid in the cold sintering of LCO. ∼95% dense 0.8LCO−0.2LLZAO cold sintered composites were obtained with a high degree of texture (Lotgering factor, LF = 0.9) at the pellet surface that yielded in-plane electronic conductivity comparable to single crystals at room temperature (10^{-2} S/cm).

EXPERIMENTAL PROCEDURE

LLZAO and LCO-LLZAO ceramics were prepared via cold sintering using raw powder supplied by Toshima (LLZAO, 99.9%) and Targray (LCO, 99.9%), respectively. For LLZAO, appropriate amounts of raw powder were weighed and mixed with 5 wt % of deionized water or 5 M LiCl solution using mortar and pestle for 10 min. The mixture was then placed in a 12.75 mm diameter stainless steel die, uniaxially pressed at 385−770 MPa, initially for 10 min at room temperature, and then for 30 min between 150−300 °C (heating rate of 10 °C min^{-1}), and cooled to room temperature. For LCO-LLZAO, various compositions based on weight fractions of $1-x(LiCoO_2)-x(Li_{6.25}La_3Zr_2Al_{0.25}O_{12})$, ($x$ = 0.2, 0.3, and 0.5) were prepared. Appropriate amounts of raw materials were weighed and mixed in acetone with a mortar and pestle for 20 min until completely dry to form a well-mixed powder. 5 wt % deionized water was then added and mixed with a mortar and pestle for a further 5 min. The mixture was placed in a 12.75 mm diameter die and cold sintered with the same parameters as LLZAO ceramics. In order to remove eventual traces of water, all pressed pellets were stored in an 80 °C oven for several days before tests. Pellet density was measured through a geometric method.

X-ray diffraction (XRD) was performed on a Bruker D2 phaser. Raman spectra were recorded using an InVia confocal Raman microscope on cold sintered pellets with a 20 kW power Green laser (514.5 nm radiation) for a 10 s exposure time. Microstructures of polished sections, parallel and perpendicular to the pressing direction, were recorded using either a Philips XL 30S FEG or FEI Inspect F scanning electron microscope (SEM). To prevent charging, the polished pellet surfaces were sputtered with Au using an Agar AGB7340 manual sputter coater.

Impedance spectroscopy, IS, was performed using an Agilent E4980A impedance analyzer with an Oxford cryo system on cold sintered ceramics pellets with sputter-coated Au electrodes. The IS measurements were carried out at an applied voltage of 100 mV, over the frequency range of 20 Hz to 1 MHz. Impedance data were corrected for sample geometry (thickness/area of the sample). High-frequency instrumental-related (impedance analyzer, leads, and sample jig) inductance effects were corrected by performing a short circuit measurement. High-temperature electrical conductivity was measured in air with a 4-probe contact method using a Netzsch SBA 458 Nemesis.

X-ray Computed Tomography (X-ray CT) scans were collected using a Zeiss Xradia 620 Versa X-ray Microscope (XRM). This method was employed specifically for nondestructive three-dimensional (3D) imaging. The sample was mounted (screwed) onto a Zeiss XRM sample holder without the need for any further sample preparation. X-rays were generated from a tungsten transmission target and collected on a CCD (charge-coupled device) 16bit 2000 × 2000 pixel detector camera. Scans were collected at an X-ray tube voltage of 150 kV, a tube current of 153 μA, 23 W, and an exposure time of 7 s per projection. 2401 projections were obtained over a scan time of ∼6 h. A filter (HE2) was used to remove low-energy X-rays, an objective lens gave an optical magnification of 40×, and binning was set to 4, producing an isotropic voxel (3D pixel) size of 740 nm at a field of view of 372 μm × 372 μm. A filtered back projection method reconstructed the data, and .txm files were converted to 8-bit grayscale two-dimensional (2D) .tiff stacks using Zeiss Scout and Scan Reconstructor software. The .tiff stack is made up of a series of images of varying grayscales, where low-density materials appear darker (black), and higher-density materials appear lighter (white). The collected data were then rendered with Dragonfly software by

https://doi.org/10.1021/acsami.3c00392
ACS Appl. Mater. Interfaces 2023, 15, 20228−20239

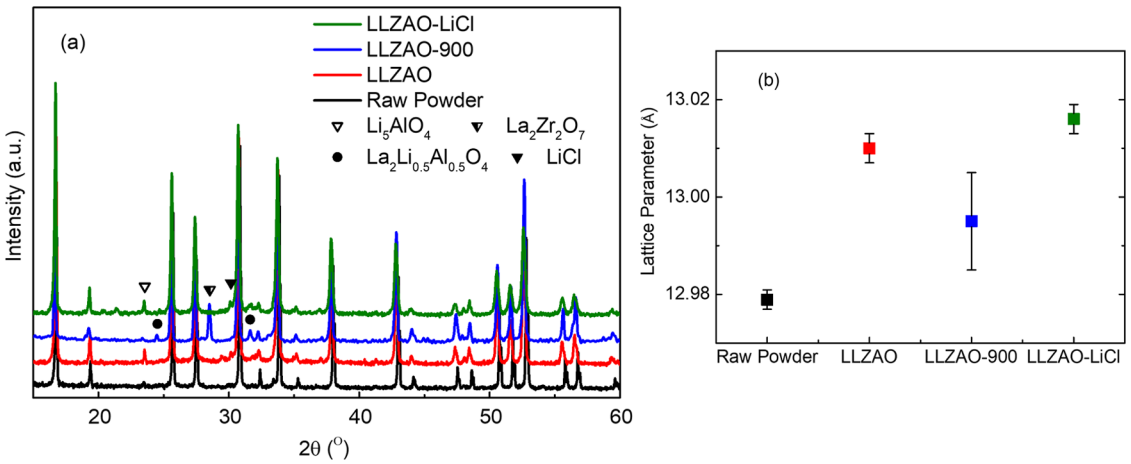

Figure 2. (a) Room temperature XRD patterns and (b) lattice parameters for raw powder, as cold sintered, 900 °C annealed, and cold sintered with LiCl LLZAO ceramics.

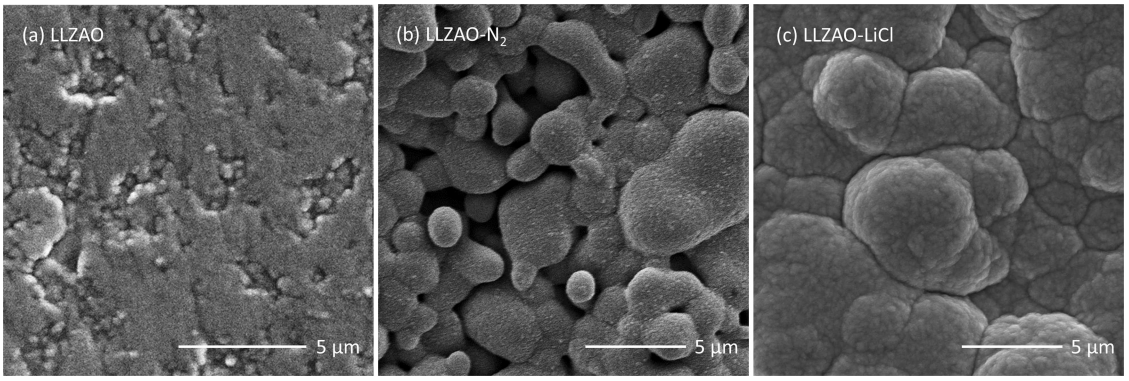

Figure 3. SEM backscattered images of variable LLZAO ceramics. (a) Cold sintered, (b) 900 °C annealed, and (c) as cold sintered with LiCl solution.

segmentation of LCO and LLZAO materials and reconstructed into a Mesh model.

RESULTS

LLZAO. *Cold Sintering LLZAO with Deionized Water.* The evolution of the relative density for LLZAO pellets with variable temperature and pressure using deionized water as a transient solvent is shown in Figure 1. The density varied from 3.86 to 4.57 g/cm^3, which is 75−87% of the theoretical value (5.10 g/cm^3), and attained a maximum at 200 °C, Figure 1a. Typically, LLZAO required a high pressure (>400 MPa), but no discernible difference was observed for pellets pressed at ∼600 and 750 MPa at 200 °C, Figure 1b. Optimum relative density (87%) was achieved at 615 MPa and 200 °C, and these conditions were used for further studies.

XRD patterns for raw powder and cold sintered LLZAO ceramics are shown in Figure 2a. Small peaks at ∼23.4 and 28.3° are associated with β-Li_5AlO_4 and $La_2Zr_2O_7$, respectively. Peaks at ∼24.5 and 31.6° are associated with the $La_2Li_{0.5}Al_{0.5}O_4$ phase. The latter two phases are associated with Li loss and are present in samples heat-treated at 900 °C, in which volatilization is expected. In contrast, peaks associated with β-Li_5AlO_4 are strongest in samples in the as-cold sintered state, which has most likely formed at the particle−particle boundaries during densification using both deionized water and LiCl solution as the transient solvent. β-Li_5AlO_4 is reported to have a low decomposition reaction energy[58] and using density functional theory (DFT) first-principles calculations, it is found to have a Li-ion conductivity on the order of 10^{-4} S/cm.[59] The lattice parameter of the cubic LLZAO phase increased slightly from ∼12.97 Å for the raw powder to ∼13.01 Å after cold sintering, Figure 2b. Backscattered scanning electron images do not reveal any noticeable secondary phases, Figure 3a. A dense microstructure can also be observed with an average grain size in the range of 0.5−1 μm.

The conductivity and electrical microstructure of LLZAO ceramics were determined using impedance spectroscopy. A large asymmetric arc was observed in complex impedance (Z^*) plots at 50 °C for LLZAO ceramics with a total resistivity, R_{total}, of 8.6 × 10^7 Ω·cm (total conductivity, $\sigma_{total} = 1/R_{total} = 1.2 \times 10^{-8}$ S/cm) taken from the low-frequency intercept of Z^* plots, Figure 4a. As-cold sintered LLZAO, therefore, not only has a high R_{total} (4 orders of magnitude greater than optimized LLZAO) but also differs due to the absence of a low-frequency Warburg diffusion spike caused by Li-ion conduction.[28] The Arrhenius plot of σ_{total} is shown in Figure 4d. The associated activation energy (E_a) is 0.75 eV, which is also significantly higher than the reported values for solid-state sintered LLZAO of ∼0.4 eV.

It is unlikely that the bulk properties of LLZAO are affected by cold sintering; however, the electrical microstructure of LLZAO is dominated by a highly insulating grain boundary, which leads to much lower σ_{total}, higher E_a, and a different electrical microstructure to solid-state sintered counterparts.

https://doi.org/10.1021/acsami.3c00392
ACS Appl. Mater. Interfaces 2023, 15, 20228−20239

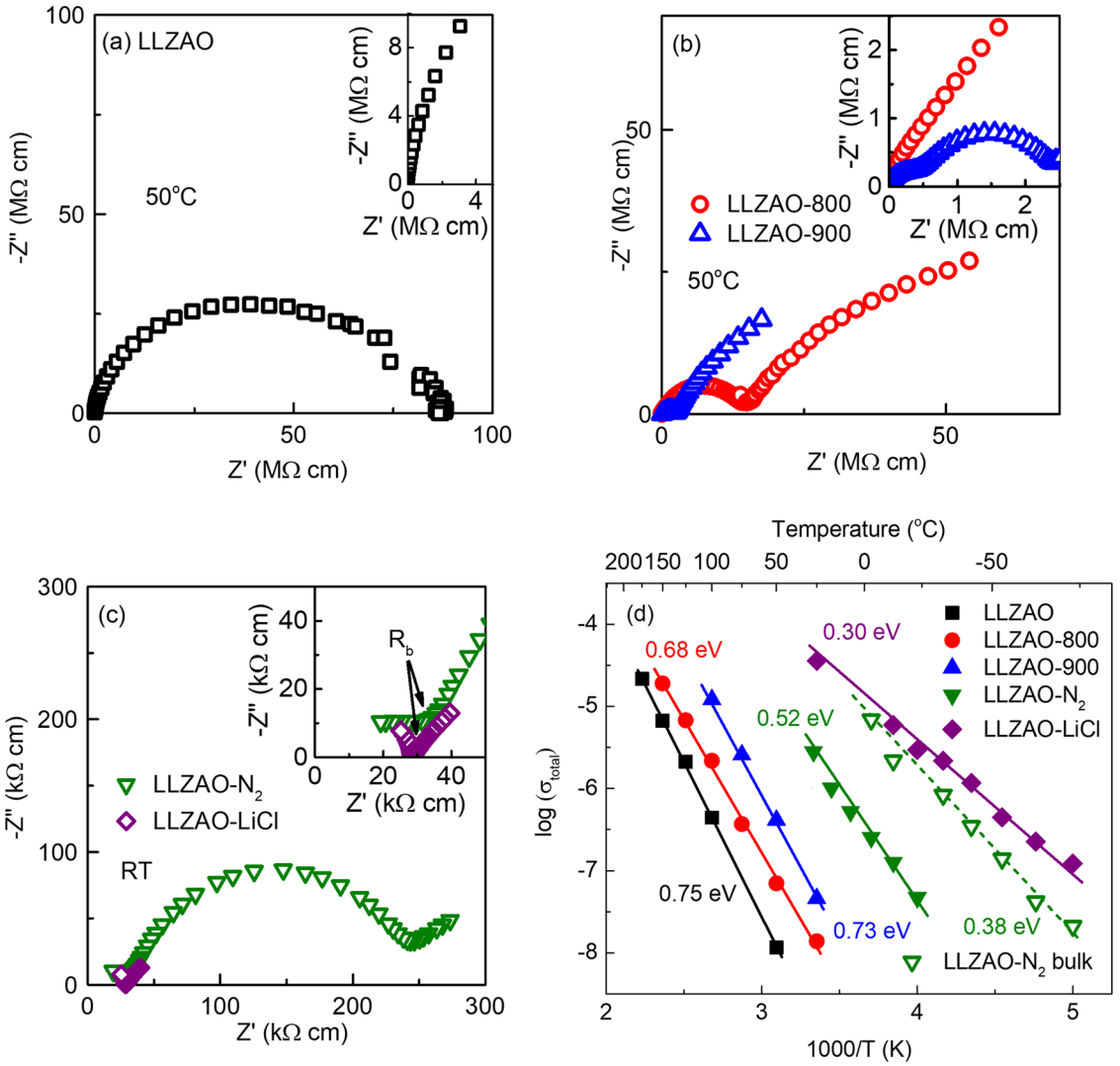

Figure 4. Z^* plots of LLZAO ceramics (a) as cold sintered, (b) post-annealed in air at 50 °C, and (c) post-annealed in N_2/cold sintered with LiCl solution at RT. (d) Arrhenius plot of total conductivity of LLZAO ceramics.

The main secondary phase peaks in XRD patterns in the as-cold sintered state arise from β-Li_5AlO_4 whose Li-ion conductivity is potentially as high as bulk LLZAO.[59] It is therefore unlikely that β-Li_5AlO_4 is the blocking layer. Instead, we propose that Li_2CO_3 is present on the surface of LLZAO powder on exposure to ambient conditions, which is then retained on densification at the particle−particle interface or grain boundaries during cold sintering, acting as a blocking layer for Li-ion conduction.[60]

Post-Annealing. To prove the hypothesis of the presence of blocking layers and improve the ionic conductivity, cold sintered LLZAO ceramics were annealed at 800/900 °C for 12 h in air (LLZAO-800 and LLZAO-900). No significant change in density was observed after annealing, as the temperature is significantly lower than that required for conventional sintering (1200 °C). The major peaks in the XRD patterns of LLZAO-900 (Figure 2a) could all be indexed according to LLZAO, but some low-intensity peaks of $La_2Zr_2O_7$ and $La_2Li_{0.5}Al_{0.5}O_4$ were observed due to Li loss at high temperatures. The lattice parameter of LLZAO-900 decreased to 12.995 ± 0.010 Å, close to the value of the starting powder, Figure 2b, and SEM did not reveal evidence of secondary phase present in XRD patterns but did show an increase in the mean grain size (1−5 μm), Figure 3b.

Impedance results for the post-annealed samples are shown in Figure 4b. R_{total} at 50 °C decreases from ~8.6 × 10^7 Ω·cm (σ_{total} = 1.2 × 10^{-8} S/cm) for as-cold sintered LLZAO to ~1.4 × 10^7 Ω·cm (σ_{total} = 7.1 × 10^{-8} S/cm) for the LLZAO-800 and finally to ~2.3 × 10^6 Ω·cm (σ_{total} = 4.3 × 10^{-7} S/cm) for the LLZAO-900. However, the associated E_a remain relatively unchanged, 0.68 and 0.73 eV for LLZAO-800 and LLZAO-900, respectively. The electrical microstructure also evolved from one single arc for LLZAO to one arc and a low-frequency spike for LLZAO-800 and a second arc with lower resistivity resolved at a high-frequency range in LLZAO-900. Each of these arcs could be modeled, to a first approximation, on a single parallel resistor−capacitor (RC) element that were connected in series. For the LLZAO-900, the associated capacitances for the three components (two arcs and one spike) from high to low frequency are 1.7, 40 pF cm^{-1} and 52 nF cm^{-1}, respectively. The three components can therefore be attributed to bulk, grain boundary, and Warburg diffusion, respectively. Samples were also post-annealed in N_2 (LLZAO-N_2) with the time extended to 24 hrs at 900 °C. Similar three electrical components were observed with R_{total} at RT further

https://doi.org/10.1021/acsami.3c00392
ACS Appl. Mater. Interfaces 2023, 15, 20228−20239

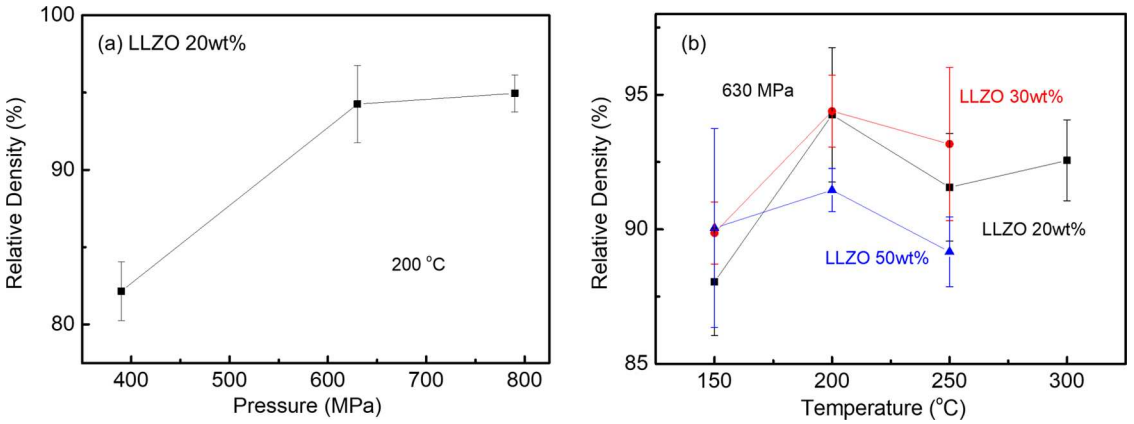

Figure 5. Relative density of LCO-LLZAO composites sintered with various (a) pressures and (b) temperatures for different amounts of LLZAO.

reduced to ~2.4×10^5 Ω·cm ($\sigma_{total} = 4.2 \times 10^{-6}$ S/cm) with E_a ~ 0.52 eV, Figure 4c,d. It is noteworthy that the bulk resistivity, R_b, of LLZAO-N_2 at RT is 3.4×10^4 Ω·cm (bulk conductivity, σ_b, = 2.9×10^{-5} S/cm) with an associated E_a of 0.38 eV (dashed line in Figure 4d), similar to the reported values for solid-state sintered LLZO-based ceramics.

We conclude, therefore, that a highly resistive grain boundary component (blocking layer) dominates R_{total} and therefore σ_{total} of cold sintered LLZAO ceramics. These observations imply that the blocking layer decomposes on heating, consistent with the presence of Li_2CO_3 at the grain boundaries within samples cold sintered using deionized water as the transient solvent. The effect of the blocking layer can be reduced by post-annealing but not eliminated even in N_2. An alternative approach is therefore proposed, in which a LiCl solution is used as the transient solvent (LLZAO-LiCl), following the same procedures described for deionized water.

Cold Sintering with LiCl Solution. The LLZAO-LiCl ceramics were first cold sintered and then annealed at 900 °C for 12 h under N_2. The relative density of LLZAO-LiCl ceramics is ~80%, lower than with deionized water. As the change of theoretical density due to the presence of LiCl is less than 1%, the theoretical density of pure LLZAO is used here for the convenience of data processing. The XRD patterns of LLZAO-LiCl show extra peaks compared to LLZAO, attributed to LiCl, Li_5AlO_4, and $La_2Zr_2O_7$ phase, Figure 2a. The calculated lattice parameter of the LLZAO phase is 13.016 ± 0.003 Å, Figure 2b, and SEM images suggest a similar particle size of 0.5−1 μm with no secondary phases observed, despite the extra peaks in XRD patterns, Figure 3c.

Z^* plots of impedance data of LLZAO-LiCl consist of a single arc and a low-frequency spike, attributed to the bulk and Warburg diffusion, respectively. The R_{total} of LLZAO-LiCl at RT extracted from the complex impedance plane is 2.8×10^4 Ω·cm ($\sigma_{total} = 3.6 \times 10^{-5}$ S/cm) with E_a of ~0.3 eV, Figure 4c,d. Without the contribution from the blocking grain boundary, the overall ionic conduction of as-cold sintered LLZAO-LiCl is therefore improved dramatically compared to LLZAO-900 processed with deionized water, approaching values associated with solid-state sintered counterparts (~$10^{-4/5}$ S/cm) and similar to σ_b for LLZAO-N_2 (2.9×10^{-5} S/cm).

LCO-LLZAO Composites. LLZAO powder was mixed into LCO powder as a binder/flux. The theoretical density of the LCO-LLZAO composites was calculated from the weight fraction of LCO and LLZAO according to

$$\bar{\rho} = \frac{w_{LCO} + w_{LLZO}}{w_{LCO}/\rho_{LCO} + w_{LCO}/\rho_{LLZO}} \quad (1)$$

where $\bar{\rho}$, ρ_{LCO}, and ρ_{LLZAO} are the theoretical densities of the composites, LCO and LLZAO and w_{LCO} and w_{LLZAO} are the weight fractions of LCO and LLZAO, respectively. Figure 5 shows the relative density of the LCO-LLZAO composite ceramics sintered with different LLZAO wt fractions, pressures, and sintering temperatures. Generally, the density of LCO-LLZAO composites increases initially with increasing pressure and temperature up to 200 °C and 630 MPa and then remains unchanged. Above 20 wt %, the wt fraction of LLZAO has little impact on the density, suggesting that the LLZAO acts as a binder/fluxing agent whose concentration should be minimized to maximize the electrical properties of the composite cathode material. 0.8LCO−0.2LLZAO cold sintered at 200 °C at 630 MPa was therefore chosen as the optimized composition for further tests and, for simplicity, will be referred to as LCO-LLZAO in the following sections.

XRD data on cold sintered ceramics revealed peaks attributed to LCO and LLZAO, Figure 6, but due to the relatively small wt %, it is not possible to establish whether the LLZAO is present as the tetragonal or cubic polymorph. The peak intensities for LCO are different from the randomly orientated powder, with significantly enhanced intensities for

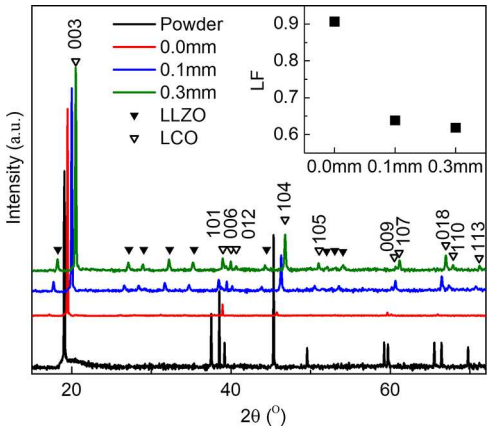

Figure 6. Room temperature XRD data of LCO powder and unpolished/polished cold sintered LCO-LLZAO ceramics. The length (x-axis) in the inset indicates the thickness of the layer removed and the associated Lotgering factor (LF).

https://doi.org/10.1021/acsami.3c00392
ACS Appl. Mater. Interfaces 2023, 15, 20228−20239

planes parallel with (001) peaks, indicating the ceramic has become textured. However, the peak intensities of polished (0.1 and 0.3 mm depth, respectively) and unpolished (0.0 mm depth) surfaces differ, illustrating the texture varies with depth away from the cold sintered surface.

The Lotgering factor (LF) indicates the degree of texture and is defined as

$$\mathrm{LF} = \frac{p - p_0}{1 - p_0} \tag{2}$$

where p is the fraction of the sum of peak intensities, which belongs to a particular orientation to that of the summation intensity of all peaks, and p_0 is p of the associated peaks from a randomly oriented sample.[61] LF = 0 and 1 correspond to random and complete orientation, respectively. The calculated LFs for LCO-LLZAO ceramics are shown in the inset of Figure 6. For an unpolished surface, LF = 0.91, but on polishing the sample surface, this decreases to ∼0.63 and 0.61 on removing 0.1 and 0.3 mm of material, respectively. The calculated lattice parameters for the LCO phase in cold sintered LCO-LLZAO are a = 2.8159 (7) Å and c = 14.049 (3) Å.

Raman spectra recorded parallel and perpendicular to the (001) direction are shown in Figure 7. Only two Raman active

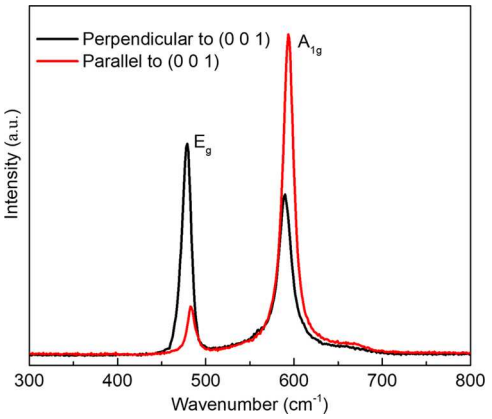

Figure 7. Raman spectra of LCO-LLZAO recorded from different orientations.

modes (E_g and A_{1g}) were observed between 300 to 800 cm^{-1}, both of which can be attributed to the LCO phase.[56] The intensity ratios of $I_{E_g}/I_{A_{1g}}$ are 0.18 and 1.3 for the parallel and perpendicular directions, respectively, thus indicating the ratio increased with a lower degree of the c-axis orientation in the latter case. Furthermore, the absence of a clear peak at 690 cm^{-1} associated with Co_3O_4 suggests this possible impurity phase is not present in cold sintered LCO-LLZAO,[62] consistent with XRD data.

Backscattered SEM images of the ceramics revealed a mixture of dark (lower weight average atomic number, WAA) LCO and bright (higher WAA) LLZAO phases. Images of the as-pressed pellet surface show that the (001) facets (highlighted) of the plate-like crystals of LCO dominate, Figure 8a,b, whereas for images obtained normal to the as-pressed surface, the (001) facets of the LCO crystals are largely absent, Figure 8c,d, consistent with XRD data. The average grain sizes are ∼5−20 and <1 μm for LCO and LLZAO, respectively.

The SEM images in Figure 8 only provide information of a 2D cross section of the microstructure of LCO-LLZAO

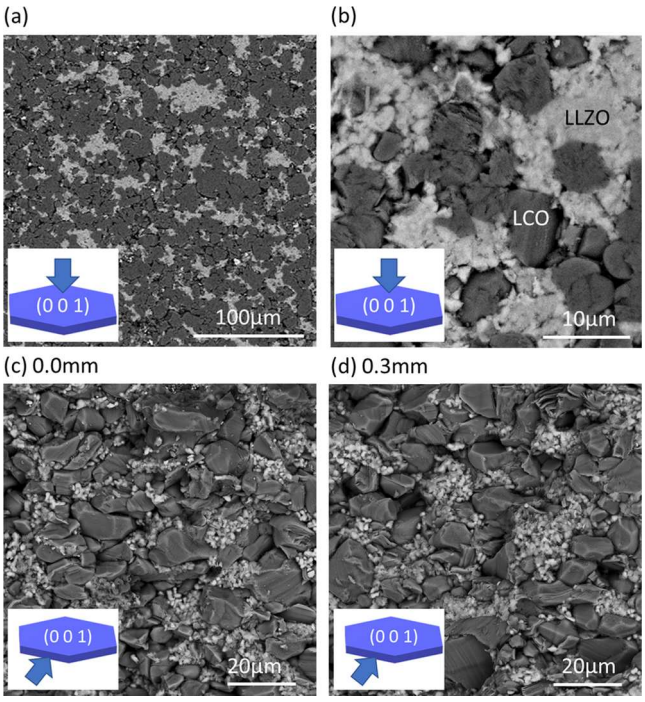

Figure 8. SEM backscattered images of LCO-LLZAO ceramic taken (a), (b) parallel and (c), (d) perpendicular to the (001) direction. Panels (c and d) are obtained from approximately 0.0 and 0.3 mm below the pellet surface, respectively.

ceramics. As an electrolyte material, the electronic conductivity in LLZAO is negligible compared to its ionic conductivity. For the LCO-LLZAO composite to work as a cathode with high electrical conductivity, it is essential to ensure the LLZAO phase has not formed a continuous blocking layer(s). 3D imaging using X-ray CT was therefore employed to determine the distribution of both phases, Figure 9. Due to the relatively low resolution of X-ray CT (voxel ∼740 nm) compared to the SEM imaging adopted in this study (nm level), LCO and LLZAO grains cannot be clearly distinguished within their clusters. Nevertheless, the two different phases can easily be identified from the X-ray CT imaging, with the lower-density (darker) areas representing LCO and higher-density (lighter) areas representing LLZAO, Figure 9a. Mesh models of both phases have then been extracted and show clearly different morphologies between the two phases. For the LLZAO phase, two morphologies have been observed, i.e., thin layers and small islands, Figure 9b. The former corresponds to LLZAO phase along the LCO grain boundary (between 2 grains), and the latter corresponds to pockets between LCO grains (3 grains or more). On the other hand, the distribution of the LCO matrix seems continuous, with some small voids, confirming the availability of pathways for electrical current.

In this study, two different methods have been adopted to measure the conductivity of the LCO-LLZAO composite: IS and a 4-probe contact method. The former is useful for establishing ionic and/or electronic conductivity and to determine the electrical microstructure of electroceramics; however, the conductivity of LCO is too high for IS above ambient temperatures. Consequently, IS and the 4-probe contact method were used below and above room temperature, respectively.

The electrical properties of LCO are anisotropic with "in-plane" (a, b plane) 500× greater than the "out-plane" (c-axis)

https://doi.org/10.1021/acsami.3c00392
ACS Appl. Mater. Interfaces 2023, 15, 20228−20239

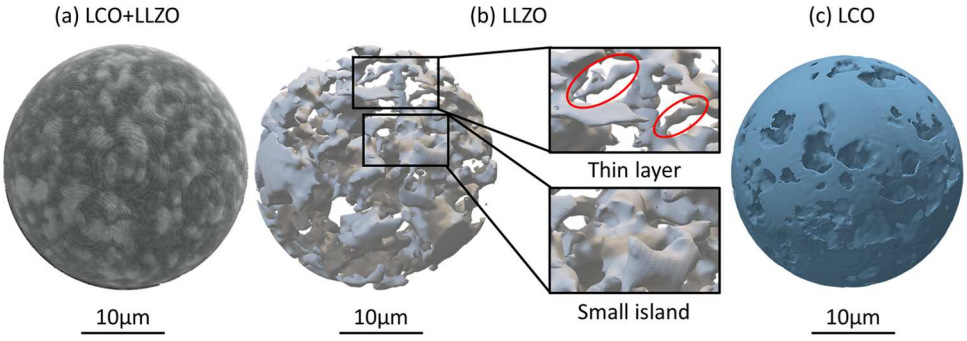

Figure 9. (a) 3D X-ray CT renderings of LCO-LLZAO composite ceramics. Mesh model of the distribution of (b) LLZAO and (c) LCO phases.

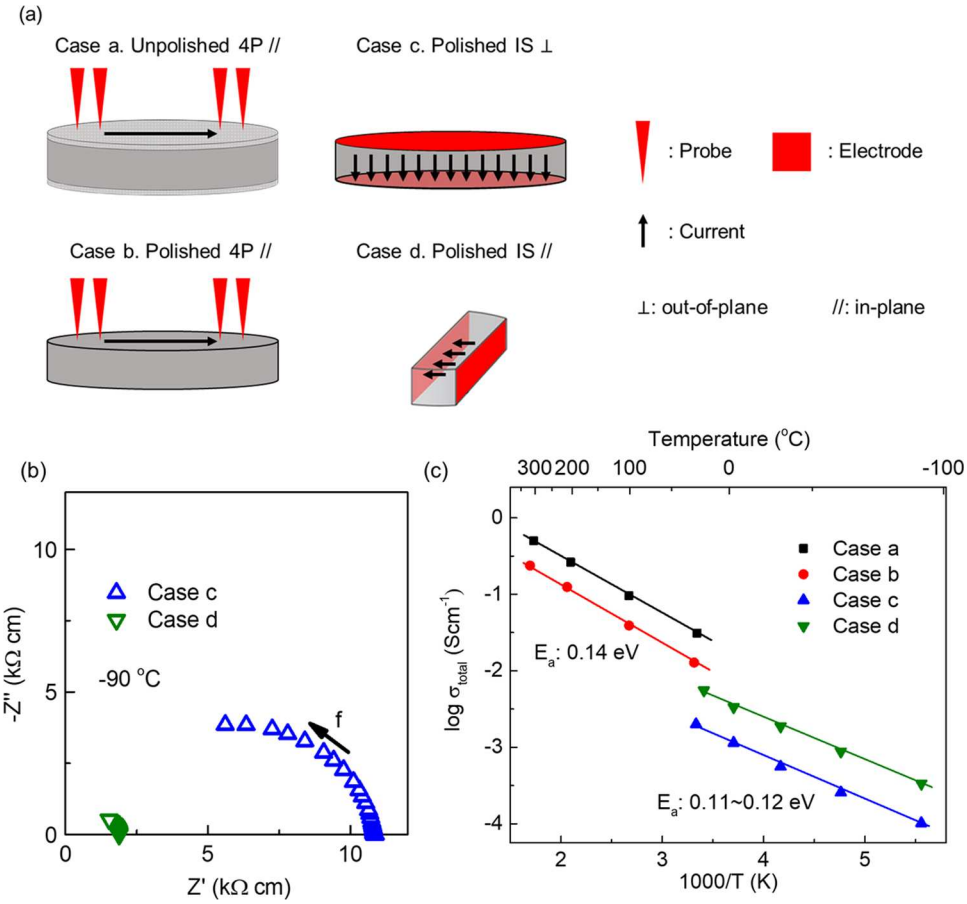

Figure 10. (a) Schematic illustrations of the experimental setups for the 4-probe method and impedance spectroscopy (polished: the top 0.1 mm layer polished off from both sides of the sample). (b) Z^* plots of polished LCO-LLZAO ceramics measured along in- and out-of-plane directions. (c) Arrhenius-type plots of total conductivity for unpolished and polished LCO-LLZAO ceramics measured along in- and out-of-plane directions.

conductivity.[53] As described above, cold sintered LCO-LLZAO pellets possess a complex microstructure with highly textured surface grains (LF = 0.91), whereas those toward the center are less oriented (LF = 0.6). The conductivity of cold sintered LCO-LLZAO ceramics, therefore, depends on both the direction and region (pellet center vs surface) measured. To distinguish the conductivity in different directions and regions, polished (0.1 mm removed) and unpolished LCO samples were measured through thickness and along their diameter. The conductivity of pellets measured through thickness is dominantly out of plane, particularly near the surface, whereas through their diameter, conductivity through the a and b plane is favored. Schematics detailing the geometry of the electrical measurements are shown in Figure 10a.

Z^* plots of polished LCO samples measured from both in- and out-plane directions are shown in Figure 10b, cases d and c, respectively. Only one incomplete arc is present in the measured temperature range (−90 to 25 °C) in both cases. The absence of a low-frequency response indicates dominant electronic conduction. The total resistivity, R_{total}, of samples were taken from the lowest frequency intercept on the Z' axis.

Total conductivity, where $\sigma_{total} = 1/R_{total}$ was extracted from impedance measurements and is shown in Figure 10c, together with σ_{total} measured on samples using the 4-probe contact method at elevated temperatures. The conductivity measured from different directions/regions of the samples shows anisotropic behavior with a maximum difference (cases a and c) of more than one order of magnitude. Similar to work

https://doi.org/10.1021/acsami.3c00392
ACS Appl. Mater. Interfaces 2023, 15, 20228−20239

reported on single crystals, out-of-plane conductivity (case c) is lower than in-plane conductivity (cases a, b, and d), with the 4-probe method on unpolished samples exhibiting the highest conductivity. The activation energy for conduction, E_a, is similar for all samples with a value of ~0.11−0.14 eV, which is characteristic of electronic conduction in LCO and agrees with the IS data.

A comparison of σ_{total} for LCO-LLZAO in this study and other studies is shown in Figure 11. All σ_{total} obtained in this

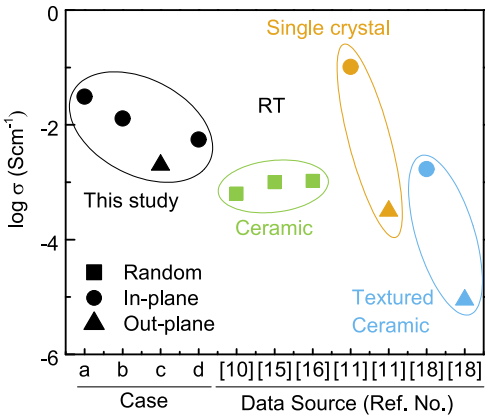

Figure 11. Comparison of room temperature conductivity of cold sintered LCO-LLZAO pellets in this study (case a: in-plane 4-probe surface layer; case b: in-plane 4-probe inner layer; case c: out-plane IS; case d: in-plane IS) with conventionally sintered LCO ceramics (random: refs 10, 15 and 16; textured: ref 18) and single crystals (ref 11).

study are high compared to previous studies, with the exception of the in-plane conductivity obtained from single crystals, which is greater (case a) by a factor of 3.[53,56,63−65] We note, however, that even the out-of-plane conductivity in our study (case c) is higher than that reported in untextured LCO ceramics prepared by a high-temperature conventional densification route. Hot pressing is known to induce texture in LCO ceramics with LF = 0.96,[56] but the conductivity remains anomalously low, suggesting other factors such as highly resistive grain boundaries may dominate the conduction properties.

DISCUSSION

LLZAO. The dissolution−precipitation mechanism associated with cold sintering is easier to achieve in systems that exhibit congruent dissolution and high solubility.[9] Xinchao et al. suggest that LLZAO undergoes only incongruent dissolution since Li^+ possesses a much higher solubility than the other constituents, La^{3+}, Al^{3+}, and Zr^{4+}.[57] As a result, a β-Li_5AlO_4 phase was observed between grains (i.e., along grain boundaries), acting in part as a binding phase, which helps densification of the ceramic. In the case of LLZAO, β-Li_5AlO_4 has also been observed in XRD as a secondary phase. We therefore propose that the high density (87%) achieved by cold sintering of LLZAO with deionized water indicates a similar mechanism in this study. However, the use of a LiCl solution partially inhibits the dissolution of Li^+ from the LLZAO particles and reduces the formation of the β-Li_5AlO_4. Simultaneously, LiCl precipitates at the particle boundary during evaporation, acting as a bond phase. The reduction in density for samples with LiCl solution rather than deionized water as the transient phase suggests that β-Li_5AlO_4 is a more effective bond phase than LiCl in the densification of LLZAO.

The starting powder and LLZAO-900 possess smaller lattice parameters than the as-cold sintered LLZAO and LLZAO-LiCl, Figure 2b. This effect is attributed to the H^+/Li^+ exchange mechanism. Larraz et al. studied the role of hydration in LLZAO and reported that the insertion of a proton causes a mild lattice expansion, which also exists in other related systems such as $Li_7La_3Sn_2O_{12}$.[26] During cold sintering of LLZAO, the insertion of a proton leads to a slight increase in lattice parameter, which is reversed on heat treatment at 900 °C as the H^+ is evolved and returns to a similar value as the starting powders.

σ_b in the LLZAO-N_2 and LLZAO-LiCl ceramics have similar values, and it is concluded that the bulk conductivity of LLZAO ceramics is largely unaffected by cold sintering, Figure 4c. In contrast, σ_{total} varies dramatically, and the associated E_a of LLZAO, LLZAO-800, and LLZAO-900 (~0.7 eV), which is dominated by an insulating grain boundary component are significantly higher than the reported values of ~0.26−0.41 eV for LLZAO ceramics, Figure 4d.[25,28,33] Due to the reduced grain boundary response, LLZAO-N_2 has an intermediate σ_{total} and E_a (0.52 eV). The smaller σ_{total} in LLZAO, LLZAO-800, LLZAO-900, and LLZAO-N_2 is therefore attributed to an insulating grain boundary component (Li_2CO_3) most likely inherent on the particle surfaces prior to densification.

LLZAO is known to rapidly form a layer of Li_2CO_3 on its surface during exposure to air, but it starts to decompose to Li_2O and CO_2 above 730 °C.[66] Conventional sintering occurs significantly above this temperature, and any residual Li_2CO_3 formed on the particle surfaces during storage and pressing is removed through decomposition and subsequent evolution of CO_2 with Li re-entering the LLZAO lattice. However, this mechanism cannot occur in cold sintered samples, and Li_2CO_3 is residual in the pellet interior for samples that use deionized water as the transient solvent. Annealing cold sintered samples at 900 °C, especially under N_2, promotes decomposition of the Li_2CO_3 and decreases the grain boundary contribution to the total resistivity, increasing the total conductivity of the samples. However, a significant grain boundary contribution still exists even in LLZAO-N_2, Figure 4c. This is mainly due to the density difference between a normal green ceramic and a cold sintered ceramic. As-pressed green bodies possess a relative density of ~60−70%. At the sintering temperature, therefore, all particle surfaces are connected via microchannels to the grain exterior, allowing egress of CO_2. However, cold sintered samples have a high relative density (~87%) before annealing; hence, egress of CO_2 from regions of closed porosity is problematic, and residual Li_2CO_3 remains at the grain boundaries.

The use of LiCl solutions rather than deionized water as a transient solvent appears to suppress the grain boundary blocking layer, virtually eliminating its contribution to σ_{total}. The mechanism for suppression of the blocking layers via LiCl solutions remains to be elucidated but may relate to the formation of an intermediate dilithium carbonate hydrochloride ($CHClLi_2O_3$)[67] compound during the unusual conditions during cold sintering. Nonetheless, the use of LiCl solutions is an effective means of cold sintering LLZAO ceramic electrolytes and could, in the future, result in a facile methodology for the fabrication of thick films suitable for the fabrication of oxide solid-state batteries.

https://doi.org/10.1021/acsami.3c00392
ACS Appl. Mater. Interfaces 2023, 15, 20228−20239

LCO-LLZAO. The conductivity of LCO-LLZAO ceramics in this study was measured via two techniques, impedance spectroscopy and a 4-probe contact method. Although they both measure R_{total}, the sampling regions are different. As illustrated in Figure 10a, the current/electric field of IS measured samples (cases c and d) goes through the whole sample, whereas for the 4-probe method, data is obtained primarily from a thin surface layer (cases a and b). The 4-probe method on unpolished samples (case a) therefore gives the highest conductivity as data are obtained only from highly textured regions (LF = 0.91) and are thus comparable with single crystals. Cases b, c, and d measure the conductivity from samples with the highly textured surface layer removed. Case b has lower conductivity than case a due to the lowering of the LF value on removal of the surface layer. We attribute the small difference in conductivity between cases b and d (same orientation) to the modest LF (~0.6), which develops in the interior of the pellet during cold sintering.

Comparison of LCO conductivity in this study to previous work indicates the LLZAO phase has not formed a blocking layer, which confirms the results from SEM and X-ray CT, Figures 8 and 9, respectively. Moreover, despite an LF ~0.6 in the pellet center, the out-of-plane conductivity measured in case c is higher than for conventionally sintered LCO ceramics with LF ~ 0. This result cannot be explained through texture, which predicts a lower conductivity, Figure 11, indicating the enhancement of conductivity must be due to another/other factor(s). One possible source could be the presence of highly conducting Co_3O_4 formed during the CSP; however, Raman spectroscopy showed no evidence of the presence of this phase, Figure 7. Two other plausible mechanisms are: (i) a space charge model and (ii) a change in the Li concentration in the LCO main phase.

Space Charge Model. Enhanced ionic conductivity has been widely observed in two-phase solid systems based on a space charge layer (SCL) at the interfaces between the different phases, i.e., an ionic conductor with an insulator or two ionic conductors. Liang et al. demonstrated that addition of Al_2O_3 to LiI increases the ionic conductivity by a factor of ~50 at room temperature.[68] Maier et al. subsequently discussed the mechanism of enhancement of ion transport in the SCL region,[69−71] and Braun et al. derived a mathematical model for the SCL formation from first principles.[72] Over several decades, there have been various reports of the SCL effect on a variety of ionically conducting materials, i.e., not limited to Li-based materials. In our study, the fine-scale distribution of the LLZAO phase with the LCO matrix, combined with the fact that LLZAO itself can exhibit high levels of Li-ion conduction, could generate SCLs in these composite ceramics.

Li-Ion Concentration Model. During cold sintering, a small fraction of Li-ions could leach into the water and may not re-enter the LCO lattice due to the low processing temperature of 200 °C. The LCO matrix may become Li-deficient with charge balance maintained by either creation of oxygen vacancies, interstitial cations (Li/Co), or the formation of electron holes. The first two mechanisms are improbable as both require relatively high energy of formation (temperature) to obtain and have negligible influence on the conductivity at room temperature. In contrast, the third mechanism is generated via a well-known low-energy process common in cobaltates in which there is an increase in transition-metal valence from 3+ to 4+, according to the following equations:

$$Li^+ = h^+ + Li(s)$$

$$Co^{3+} + h^+ = Co^{4+}$$

The oxidation of LCO should lead to enhanced p-type conduction due to an increase in the mixed oxidation state Co^{3+} and Co^{4+} ions. Ménétrier et al. proposed a relationship between Li concentration and the lattice parameter of LCO[73] for which our study (a = 2.8159 (7) Å and c = 14.049 (3) Å) suggests a Li stoichiometry of ~0.98−1.00 and therefore indicates only low Li loss (if any) during the CSP. Nonetheless, the greater sensitivity of electrical measurements to variations in p-type conductivity is consistent with the Li-ion concentration model.

These two mechanisms are not necessarily mutually exclusive, and improvement in both electronic and ionic conduction is possible. However, the absence of a low-frequency spike in the Z^* plots, Figure 10b, is an indicator of Warburg diffusion, and therefore, ion migration at the sample/electrode interface indicates the conduction is predominately electronic. Furthermore, the low E_a associated with σ_{total} also supports a model based primarily on electronic conduction. Therefore, the space charge model is unlikely to be the sole mechanism responsible for enhanced conductivity.

It has been suggested the temperature-dependent in-plane conductivity of LCO is consistent with a variable range-hopping (VRH) mechanism instead of the normal activation (Arrhenius-type) mechanism. Takahashi et al.[53] reported a two-dimensional (2D) VRH mechanism for single crystals, whereas Zhang et al.[56] reported a three-dimensional (3D) VRH mechanism for highly textured ceramics. The latter attributed the 3D VRH mechanism to the role of grain boundaries and/or the nonperfect alignment of grains in their textured ceramics. According to VRH theory, the conduction should obey

$$\sigma = \sigma_0 e^{-(T_0/T)^{1/(d+1)}}$$

where d is the dimension of the conduction path and T_0 is the Mott characteristic temperature. The conductivity data in this study were therefore plotted against $1000/T$, $T^{-1/3}$, and $T^{-1/4}$ to verify which mechanism(s) is adopted in cold sintered samples, Figures S1 and S2. Based on the residual sum of squares (RSS) associated with linear fitting, the sub-ambient conductivity data of both in- and out-of-plane conductivity is consistent with a VRH mechanism. The out-of-plane conductivity (case c) shows a better fit for 3D VRH, whereas it is difficult to decipher between 2D and 3D VRH for the in-plane conductivity (case d) due to the lack of data points. The in-plane conductivity was remeasured to collect additional data, Figure S3, and fitting to 3D VRH generates a lower RSS than to 2D VRH. In contrast, the RSS of in-plane conductivity at elevated temperatures (cases a and b) has its lowest value when plotted against $1000/T$, Figure S2. This indicates the in-plane conductivity of cold sintered LCO-LLZAO composites at higher temperatures is better described by the normal activation process rather than VRH.

CONCLUSIONS

The present work suggests densification of LLZAO via an aqueous cold sintering approach is not only feasible but can also achieve conduction similar to that of the bulk (~3×10^{-5} S/cm) or raw powder (i.e., no other resistive component introduced) if a LiCl solution is used instead of deionized

https://doi.org/10.1021/acsami.3c00392
ACS Appl. Mater. Interfaces 2023, 15, 20228−20239

water. If only deionized water is utilized, the relative densities (87%) of cold sintered samples are higher, but highly insulating grain boundary blocking layers form, which are not completely eliminated even after a post-cold sinter anneal at 900 °C in N_2.

Using LLZAO as a flux/binder, LCO-LLZAO ceramics were successfully fabricated with a high relative density of >95% at a low sintering temperature of 200 °C, with a pressure of 630 MPa and water as the transient liquid. The LLZAO phase disperses homogeneously in the LCO matrix without forming any significant blocking layer(s). A highly textured surface (LF = 0.91) was observed after CSP, but the level of orientation decreased with depth into the ceramic. Electrical characterization, including impedance spectroscopy and 4-probe resistivity at various temperatures, shows enhanced electronic conductivity compared to LCO ceramics synthesized via other routes and is primarily attributed to partial oxidation of Co-ions due to Li loss during CSP of LCO-LLZAO. A one order of magnitude anisotropy between in-plane and out-of-plane conductivity was obtained. The temperature-dependent conductivity was consistent with 3D VRH and normal (Arrhenius) activation-type behavior for sub-ambient and elevated temperatures, respectively.

■ ASSOCIATED CONTENT

Supporting Information

The Supporting Information is available free of charge at https://pubs.acs.org/doi/10.1021/acsami.3c00392.

VRH and Arrhenius-type plots for conductivity measured by diffrerent experimental setups (PDF)

■ AUTHOR INFORMATION

Corresponding Author

Ian M. Reaney − *Department of Materials Science and Engineering, University of Sheffield, Sheffield S1 3JD, U.K.;* orcid.org/0000-0003-3893-6544; Email: i.m.reaney@sheffield.ac.uk

Authors

Linhao Li − *College of Mathematics and Physics, Beijing University of Chemical Technology, Beijing 100029, China; Department of Materials Science and Engineering, University of Sheffield, Sheffield S1 3JD, U.K.;* orcid.org/0000-0002-9565-9830

Jessica Andrews − *Department of Materials Science and Engineering, University of Sheffield, Sheffield S1 3JD, U.K.*

Ria Mitchell − *Department of Materials Science and Engineering, University of Sheffield, Sheffield S1 3JD, U.K.;* orcid.org/0000-0002-6328-3998

Daniel Button − *Department of Materials Science and Engineering, University of Sheffield, Sheffield S1 3JD, U.K.*

Derek C. Sinclair − *Department of Materials Science and Engineering, University of Sheffield, Sheffield S1 3JD, U.K.;* orcid.org/0000-0002-8031-7678

Complete contact information is available at: https://pubs.acs.org/10.1021/acsami.3c00392

Notes

The authors declare no competing financial interest.

■ ACKNOWLEDGMENTS

The authors thank the EPSRC for funding aspects of this work from "Substitution and Sustainability in Functional Materials and Devices" (EP/L017563/1) and Sheffield Tomography Center (STC) funding from "An X-ray Micro-Computed Tomography Facility with in situ/in operando testing" (EP/T006390/1). The authors would like to acknowledge support from the InnovateUK grants: "Cathodes, Anodes, and Solid-state Electrolytes for Lithium Ion Batteries, CASELIBs" (TS/S023143/1) and "Cold Sintering of Cathodes and Solid Electrolytes, CSiCASE" (TS/V01398X/1). Prof. Beverley Inkson and Brendan Player (University of Sheffield) are acknowledged for helpful discussions and advice on X-ray CT measurement and analysis. Dr. Enrico Petrucco and Dr. Chris Nuttall (Johnson Matthey plc) are acknowledged for providing LCO powder and pertinent insights. The authors wish to thank Ge Wang, Dawei Wang, and Zhilun Lu for their help with cold sintering, sample preparation, and scanning electron microscopy, respectively.

■ REFERENCES

(1) Armand, M.; Tarascon, J. M. Building Better Batteries. *Nature* **2008**, *451*, 652−657.

(2) Larcher, D.; Tarascon, J.-M. Towards Greener and More Sustainable Batteries for Electrical Energy Storage. *Nat. Chem.* **2015**, *7*, 19−29.

(3) Guo, J.; Guo, H.; Baker, A. L.; Lanagan, M. T.; Kupp, E. R.; Messing, G. L.; Randall, C. A. Cold Sintering: A Paradigm Shift for Processing and Integration of Ceramics. *Angew. Chem.* **2016**, *128*, 11629−11633.

(4) Guo, J.; Baker, A. L.; Guo, H.; Lanagan, M.; Randall, C. A. Cold Sintering Process: A New Era for Ceramic Packaging and Microwave Device Development. *J. Am. Ceram. Soc.* **2017**, *100*, 669−677.

(5) Guo, J.; Floyd, R.; Lowum, S.; Maria, J.-P.; de Beauvoir, T. H.; Seo, J.-H.; Randall, C. A. Cold Sintering: Progress, Challenges, and Future Opportunities. *Annu. Rev. Mater. Res.* **2019**, *49*, 275−295.

(6) Ibn-Mohammed, T.; Randall, C. A.; Mustapha, K. B.; Guo, J.; Walker, J.; Berbano, S.; Koh, S. C. L.; Wang, D.; Sinclair, D. C.; Reaney, I. M. Decarbonising Ceramic Manufacturing: A Techno-Economic Analysis of Energy Efficient Sintering Technologies in the Functional Materials Sector. *J. Eur. Ceram. Soc.* **2019**, *39*, 5213−5235.

(7) Funahashi, S.; Guo, J.; Guo, H.; Wang, K.; Baker, A. L.; Shiratsuyu, K.; Randall, C. A. Demonstration of the Cold Sintering Process Study for the Densification and Grain Growth of ZnO Ceramics. *J. Am. Ceram. Soc.* **2017**, *100*, 546−553.

(8) Tsuji, K.; Ndayishimiye, A.; Lowum, S.; Floyd, R.; Wang, K.; Wetherington, M.; Maria, J. P.; Randall, C. A. Single Step Densification of High Permittivity $BaTiO_3$ Ceramics at 300 °C. *J. Eur. Ceram. Soc.* **2020**, *40*, 1280−1284.

(9) Wang, D.; Li, L.; Jiang, J.; Lu, Z.; Wang, G.; Song, K.; Zhou, D.; Reaney, I. M. Cold Sintering of Microwave Dielectric Ceramics and Devices. *J. Mater. Res.* **2021**, *36*, 333−349.

(10) Wang, D.; Zhou, D.; Zhang, S.; Vardaxoglou, Y.; Whittow, W. G.; Cadman, D.; Reaney, I. M. Cold-Sintered Temperature Stable $Na_{0.5}Bi_{0.5}MoO_4$-Li_2MoO_4 Microwave Composite Ceramics. *ACS Sustainable Chem. Eng.* **2018**, *6*, 2438−2444.

(11) Liu, Y.; Sun, Q.; Wang, D.; Adair, K.; Liang, J.; Sun, X. Development of the Cold Sintering Process and Its Application in Solid-State Lithium Batteries. *J. Power Sources* **2018**, *393*, 193−203.

(12) Seo, J. H.; Verlinde, K.; Guo, J.; Heidary, D. S. B.; Rajagopalan, R.; Mallouk, T. E.; Randall, C. A. Cold Sintering Approach to Fabrication of High Rate Performance Binderless $LiFePO_4$ Cathode with High Volumetric Capacity. *Scr. Mater.* **2018**, *146*, 267−271.

(13) Zeng, D.; Yao, J.; Zhang, L.; Xu, R.; Wang, S.; Yan, X.; Yu, C.; Wang, L. Promoting Favorable Interfacial Properties in Lithium-Based

Batteries Using Chlorine-Rich Sulfide Inorganic Solid-State Electrolytes. *Nat. Commun.* **2022**, *13*, No. 1909.
(14) Zaengle, T. H.; Ndayishimiye, A.; Tsuji, K.; Fan, Z.; Bang, S. H.; Perini, J.; Misture, S. T.; Randall, C. A. Single-step Densification of Nanocrystalline CeO_2 by the Cold Sintering Process. *J. Am. Ceram. Soc.* **2020**, *103*, 2979−2985.
(15) Zhou, D.; Pang, L. X.; Wang, D. W.; Reaney, I. M. Novel Water-Assisting Low Firing MoO_3 Microwave Dielectric Ceramics. *J. Eur. Ceram. Soc.* **2019**, *39*, 2374−2378.
(16) Guo, H.; Bayer, T. J. M.; Guo, J.; Baker, A.; Randall, C. A. Cold Sintering Process for 8 Mol%Y_2O_3-Stabilized ZrO_2 Ceramics. *J. Eur. Ceram. Soc.* **2017**, *37*, 2303−2308.
(17) Ji, Y.; Song, K.; Zhang, S.; Lu, Z.; Wang, G.; Li, L.; Zhou, D.; Wang, D.; Reaney, I. M. Cold Sintered, Temperature-Stable $CaSnSiO_5$-K_2MoO_4 Composite Microwave Ceramics and Its Prototype Microstrip Patch Antenna. *J. Eur. Ceram. Soc.* **2021**, *41*, 424−429.
(18) Huang, H. Q.; Tang, J.; Liu, J. Preparation of $Na_{0.5}Bi_{0.5}TiO_3$ Ceramics by Hydrothermal-Assisted Cold Sintering. *Ceram. Int.* **2019**, *45*, 6753−6758.
(19) Seo, J. H.; Guo, J.; Guo, H.; Verlinde, K.; Heidary, D. S. B.; Rajagopalan, R.; Randall, C. A. Cold Sintering of a Li-Ion Cathode: $LiFePO_4$-Composite with High Volumetric Capacity. *Ceram. Int.* **2017**, *43*, 15370−15374.
(20) Faouri, S. S.; Mostaed, A.; Dean, J. S.; Wang, D.; Sinclair, D. C.; Zhang, S.; Whittow, W. G.; Vardaxoglou, Y.; Reaney, I. M. High Quality Factor Cold Sintered Li_2MoO_4 −$BaFe_{12}O_{19}$ Composites for Microwave Applications. *Acta Mater.* **2019**, *166*, 202−207.
(21) Seo, J. H.; Nakaya, H.; Takeuchi, Y.; Fan, Z.; Hikosaka, H.; Rajagopalan, R.; Gomez, E. D.; Iwasaki, M.; Randall, C. A. Broad Temperature Dependence, High Conductivity, and Structure-Property Relations of Cold Sintering of LLZO-Based Composite Electrolytes. *J. Eur. Ceram. Soc.* **2020**, *40*, 6241−6248.
(22) Song, R.; Yao, J.; Xu, R.; Li, Z.; Yan, X.; Yu, C.; Huang, Z.; Zhang, L. Metastable Decomposition Realizing Dendrite-Free Solid-State Li Metal Batteries. *Adv. Energy Mater.* **2023**, *13*, No. 2203631.
(23) Murugan, R.; Thangadurai, V.; Weppner, W. Fast Lithium Ion Conduction in Garnet-Type $Li_7La_3Zr_2O_{12}$. *Angew. Chem., Int. Ed.* **2007**, *46*, 7778−7781.
(24) Awaka, J.; Kijima, N.; Hayakawa, H.; Akimoto, J. Synthesis and Structure Analysis of Tetragonal $Li_7La_3Zr_2O_{12}$ with the Garnet-Related Type Structure. *J. Solid State Chem.* **2009**, *182*, 2046−2052.
(25) Wolfenstine, J.; Rangasamy, E.; Allen, J. L.; Sakamoto, J. High Conductivity of Dense Tetragonal $Li_7La_3Zr_2O_{12}$. *J. Power Sources* **2012**, *208*, 193−196.
(26) Larraz, G.; Orera, A.; Sanjuán, M. L. Cubic Phases of Garnet-Type $Li_7La_3Zr_2O_{12}$: The Role of Hydration. *J. Mater. Chem. A* **2013**, *1*, 11419−11428.
(27) Thompson, T.; Wolfenstine, J.; Allen, J. L.; Johannes, M.; Huq, A.; David, I. N.; Sakamoto, J. Tetragonal vs. Cubic Phase Stability in Al − Free Ta Doped $Li_7La_3Zr_2O_{12}$ (LLZO). *J. Mater. Chem. A* **2014**, *2*, 13431−13436.
(28) Rangasamy, E.; Wolfenstine, J.; Sakamoto, J. The Role of Al and Li Concentration on the Formation of Cubic Garnet Solid Electrolyte of Nominal Composition $Li_7La_3Zr_2O_{12}$. *Solid State Ionics* **2012**, *206*, 28−32.
(29) Wolfenstine, J.; Ratchford, J.; Rangasamy, E.; Sakamoto, J.; Allen, J. L. Synthesis and High Li-Ion Conductivity of Ga-Stabilized Cubic $Li_7La_3Zr_2O_{12}$. *Mater. Chem. Phys.* **2012**, *134*, 571−575.
(30) Rettenwander, D.; Geiger, C. A.; Amthauer, G. Synthesis and Crystal Chemistry of the Fast Li-Ion Conductor $Li_7La_3Zr_2O_{12}$ Doped with Fe. *Inorg. Chem.* **2013**, *52*, 8005−8009.
(31) Logéat, A.; Köhler, T.; Eisele, U.; Stiaszny, B.; Harzer, A.; Tovar, M.; Senyshyn, A.; Ehrenberg, H.; Kozinsky, B. From Order to Disorder: The Structure of Lithium-Conducting Garnets $Li_{7-x}La_3Ta_xZr_{2-x}O_{12}$ (x = 0−2). *Solid State Ionics* **2012**, *206*, 33−38.
(32) Kihira, Y.; Ohta, S.; Imagawa, H.; Asaoka, T. Effect of Simultaneous Substitution of Alkali Earth Metals and Nb in $Li_7La_3Zr_2O_{12}$ on Lithium-Ion Conductivity. *ECS Electrochem. Lett.* **2013**, *2*, No. A56.
(33) Ramakumar, S.; Satyanarayana, L.; Manorama, S. V.; Murugan, R. Structure and Li+ Dynamics of Sb-Doped $Li_7La_3Zr_2O_{12}$ Fast Lithium Ion Conductors. *Phys. Chem. Chem. Phys.* **2013**, *15*, 11327−11338.
(34) Kotobuki, M.; Kanamura, K.; Sato, Y.; Yoshida, T. Fabrication of All-Solid-State Lithium Battery with Lithium Metal Anode Using Al_2O_3-Added $Li_7La_3Zr_2O_{12}$ Solid Electrolyte. *J. Power Sources* **2011**, *196*, 7750−7754.
(35) Ohta, S.; Kobayashi, T.; Asaoka, T. High Lithium Ionic Conductivity in the Garnet-Type Oxide $Li_{7-X}La_3(Zr_{2-X},Nb_X)O_{12}$ (X = 0-2). *J. Power Sources* **2011**, *196*, 3342−3345.
(36) Murugan, R.; Ramakumar, S.; Janani, N. High Conductive Yttrium Doped $Li_7La_3Zr_2O_{12}$ Cubic Lithium Garnet. *Electrochem. Commun.* **2011**, *13*, 1373−1375.
(37) Zhang, Y. Rapid Fabrication of of $Li_7La_3Zr_2O_{12}$ Solid Electrolyte with Enhanced Lithium Ionic Conductivity by Microwave Sintering. *Int. J. Electrochem. Sci.* **2020**, *15*, 7163−7174.
(38) Ren, Y.; Chen, K.; Chen, R.; Liu, T.; Zhang, Y.; Nan, C. W. Oxide Electrolytes for Lithium Batteries. *J. Am. Ceram. Soc.* **2015**, *98*, 3603−3623.
(39) Geiger, C. A.; Alekseev, E.; Lazic, B.; Fisch, M.; Armbruster, T.; Langner, R.; Fechtelkord, M.; Kim, N.; Pettke, T.; Weppner, W. Crystal Chemistry and Stability of "$Li_7La_3Zr_2O_{12}$" Garnet: A Fast Lithium-Ion Conductor. *Inorg. Chem.* **2011**, *50*, 1089−1097.
(40) Bernstein, N.; Johannes, M. D.; Hoang, K. Origin of the Structural Phase Transition in $Li_7La_3Zr_2O_{12}$. *Phys. Rev. Lett.* **2012**, *109*, No. 205702.
(41) Zhang, Z.; Zhang, L.; Yu, C.; Yan, X.; Xu, B.; Wang, L. Lithium Halide Coating as an Effective Intergrain Engineering for Garnet-Type Solid Electrolytes Avoiding High Temperature Sintering. *Electrochim. Acta* **2018**, *289*, 254−263.
(42) Mizushima, K.; Jones, P.; Wiseman, P.; Goodenough, J. $LixCoO_2$ ($0<x\leqslant 1$): A New Cathode Material for Batteries of High Energy Density. *Solid State Ionics* **1981**, *3*−*4*, 171−174.
(43) Goodenough, J. B.; Kim, Y. Challenges for Rechargeable Li Batteries. *Chem. Mater.* **2010**, *22*, 587−603.
(44) Wang, K.; Wan, J.; Xiang, Y.; Zhu, J.; Leng, Q.; Wang, M.; Xu, L.; Yang, Y. Recent Advances and Historical Developments of High Voltage Lithium Cobalt Oxide Materials for Rechargeable Li-Ion Batteries. *J. Power Sources* **2020**, *460*, No. 228062.
(45) Wang, X.; Wang, X.; Lu, Y. Realizing High Voltage Lithium Cobalt Oxide in Lithium-Ion Batteries. *Ind. Eng. Chem. Res.* **2019**, *58*, 10119−10139.
(46) Thackeray, M. M.; Johnson, P. J.; de Picciotto, L. A.; Bruce, P. G.; Goodenough, J. B. Electrochemical Extraction of Lithium from $LiMn_2O_4$. *Mater. Res. Bull.* **1984**, *19*, 179−187.
(47) Qian, R.; Liu, Y.; Cheng, T.; Li, P.; Chen, R.; Lyu, Y.; Guo, B. Enhanced Surface Chemical and Structural Stability of Ni-Rich Cathode Materials by Synchronous Lithium-Ion Conductor Coating for Lithium-Ion Batteries. *ACS Appl. Mater. Interfaces* **2020**, *12*, 13813−13823.
(48) Bianchini, M.; Roca-Ayats, M.; Hartmann, P.; Brezesinski, T.; Janek, J. There and Back Again—The Journey of $LiNiO_2$ as a Cathode Active Material. *Angew. Chem., Int. Ed.* **2019**, *58*, 10434−10458.
(49) Zheng, J.; Myeong, S.; Cho, W.; Yan, P.; Xiao, J.; Wang, C.; Cho, J.; Zhang, J. Li- and Mn-Rich Cathode Materials: Challenges to Commercialization. *Adv. Energy Mater.* **2017**, *7*, No. 1601284.
(50) Padhi, A. K.; Nanjundaswamy, K. S.; Goodenough, J. B. Phospho-olivines as Positive-Electrode Materials for Rechargeable Lithium Batteries. *J. Electrochem. Soc.* **1997**, *144*, 1188−1194.
(51) Negi, R. S.; Culver, S. P.; Mazilkin, A.; Brezesinski, T.; Elm, M. T. Enhancing the Electrochemical Performance of Li-$Ni_{0.70}Co_{0.15}Mn_{0.15}O_2$ Cathodes Using a Practical Solution-Based Al_2O_3 Coating. *ACS Appl. Mater. Interfaces* **2020**, *12*, 31392−31400.
(52) Zahnow, J.; Bernges, T.; Wagner, A.; Bohn, N.; Binder, J. R.; Zeier, W. G.; Elm, M. T.; Janek, J. Impedance Analysis of NCM Cathode Materials: Electronic and Ionic Partial Conductivities and

https://doi.org/10.1021/acsami.3c00392
ACS Appl. Mater. Interfaces 2023, 15, 20228−20239

the Influence of Microstructure. *ACS Appl. Energy Mater.* **2021**, *4*, 1335−1345.
(53) Takahashi, Y.; Gotoh, Y.; Akimoto, J.; Mizuta, S.; Tokiwa, K.; Watanabe, T. Anisotropic Electrical Conductivity in $LiCoO_2$ Single Crystal. *J. Solid State Chem.* **2002**, *164*, 1−4.
(54) Yamada, H.; Suzuki, T. S.; Uchikoshi, T.; Hozumi, M.; Kohama, K.; Sakka, Y. Fabrication and Analysis of the Oriented $LiCoO_2$ by Slip Casting in a Strong Magnetic Field. *J. Am. Ceram. Soc.* **2012**, *95*, 3428−3433.
(55) Yamada, H.; Suzuki, T. S.; Uchikoshi, T.; Hozumi, M.; Saito, T.; Sakka, Y. Anisotropy in Activation Energy of Textured $LiCoO_2$ for the Initial Stage of Sintering. *J. Eur. Ceram. Soc.* **2013**, *33*, 1037−1044.
(56) Zhang, H.; Baker, P. J.; Grant, P. S. Fabrication and Electrical Properties of Bulk Textured $LiCoO_2$. *J. Am. Ceram. Soc.* **2010**, *93*, 1856−1859.
(57) Wang, X.; Wang, J.; Li, F.; Zhu, F.; Ma, C. Influence of Cold Sintering Process on the Structure and Properties of Garnet-Type Solid Electrolytes. *Ceram. Int.* **2020**, *46*, 18544−18550.
(58) Gao, B.; Jalem, R.; Tateyama, Y. Atomistic Insight into the Dopant Impacts at the Garnet $Li_7La_3Zr_2O_{12}$ Solid Electrolyte Grain Boundaries. *J. Mater. Chem. A* **2022**, *10*, 10083−10091.
(59) Zhang, B.; Zhong, J.; Pan, F.; Lin, Z. Potential Solid-State Electrolytes with Good Balance between Ionic Conductivity and Electrochemical Stability: $Li_{5-x}M_{1-x}M'_xO_4$ (M = Al and Ga and M′ = Si and Ge). *ACS Appl. Mater. Interfaces* **2021**, *13*, 61296−61304.
(60) Sharafi, A.; Yu, S.; Naguib, M.; Lee, M.; Ma, C.; Meyer, H. M.; Nanda, J.; Chi, M.; Siegel, D. J.; Sakamoto, J. Impact of Air Exposure and Surface Chemistry on Li-$Li_7La_3Zr_2O_{12}$ Interfacial Resistance. *J. Mater. Chem. A* **2017**, *5*, 13475−13487.
(61) Furushima, R.; Tanaka, S.; Kato, Z.; Uematsu, K. Orientation Distribution−Lotgering Factor Relationship in a Polycrystalline Material—as an Example of Bismuth Titanate Prepared by a Magnetic Field. *J. Ceram. Soc. Jpn.* **2010**, *118*, 921−926.
(62) Iriyama, Y.; Inaba, M.; Abe, T.; Ogumi, Z. Preparation of C-Axis Oriented Thin Films of $LiCoO_2$ by Pulsed Laser Deposition and Their Electrochemical Properties. *J. Power Sources* **2001**, *94*, 175−182.
(63) Tukamoto, H.; West, A. R. Electronic Conductivity of $LiCoO_2$ and Its Enhancement by Magnesium Doping. *J. Electrochem. Soc.* **1997**, *144*, 3164−3168.
(64) Ohta, N.; Takada, K.; Sakaguchi, I.; Zhang, L.; Ma, R.; Fukuda, K.; Osada, M.; Sasaki, T. $LiNbO_3$-Coated $LiCoO_2$ as Cathode Material for All Solid-State Lithium Secondary Batteries. *Electrochem. Commun.* **2007**, *9*, 1486−1490.
(65) Cao, Q.; Zhang, H. P.; Wang, G. J.; Xia, Q.; Wu, Y. P.; Wu, H. Q. A Novel Carbon-Coated $LiCoO_2$ as Cathode Material for Lithium Ion Battery. *Electrochem. Commun.* **2007**, *9*, 1228−1232.
(66) Shi, L.; Qu, T.; Liu, D.; Deng, Y.; Yang, B.; Dai, Y. Process of Thermal Decomposition of Lithium Carbonate. *Miner., Met. Mater. Ser.* **2020**, 107−116.
(67) Lithium Chloride Lithium CarbonatelCHClLi2O3—PubChem, 2022. https://pubchem.ncbi.nlm.nih.gov/compound/Lithium-chloride-lithium-carbonate. (accessed August 29, 2022).
(68) Liang, C. C. Conduction Characteristics of the Lithium Iodide-Aluminum Oxide Solid Electrolytes. *J. Electrochem. Soc.* **1973**, *120*, 1289−1292.
(69) Maier, J. Ionic Conduction in Space Charge Regions. *Prog. Solid State Chem.* **1995**, *23*, 171−263.
(70) Maier, J. Surface Induced Defects in the Space Charge Region and the Enhancement of Ionic Conductivity in Two-Phase Systems. *Phys. Status Solidi* **1984**, *123*, K89−K91.
(71) Maier, J. Space Charge Regions in Solid Two-Phase Systems and Their Conduction Contribution—I. Conductance Enhancement in the System Ionic Conductor-'Inert' Phase and Application on AgCl:Al_2O_3 and AgCl:SiO_2. *J. Phys. Chem. Solids* **1985**, *46*, 309−320.
(72) Braun, S.; Yada, C.; Latz, A. Thermodynamically Consistent Model for Space-Charge-Layer Formation in a Solid Electrolyte. *J. Phys. Chem. C* **2015**, *119*, 22281−22288.
(73) Ménétrier, M.; Saadoune, I.; Levasseur, S.; Delmas, C. The Insulator-Metal Transition upon Lithium Deintercalation from $LiCoO_2$: Electronic Properties and 7Li NMR Study. *J. Mater. Chem.* **1999**, *9*, 1135−1140.